

See discussions, stats, and author profiles for this publication at: <https://www.researchgate.net/publication/6951954>

Resonance Hyper-Raman Excitation Profiles and Two-Photon States of a Donor–Acceptor Substituted Polyene

ARTICLE *in* THE JOURNAL OF PHYSICAL CHEMISTRY A · DECEMBER 2005

Impact Factor: 2.69 · DOI: 10.1021/jp0545851 · Source: PubMed

CITATIONS

29

READS

25

3 AUTHORS, INCLUDING:



Lian C T Shoute

University of Alberta

58 PUBLICATIONS 891 CITATIONS

SEE PROFILE

Resonance Hyper-Raman Excitation Profiles and Two-Photon States of a Donor–Acceptor Substituted Polyene

Lian C. T. Shoute,[†] Mireille Blanchard-Desce,[‡] and Anne Myers Kelley^{*,†}

School of Natural Sciences, University of California, Merced, P.O. Box 2039, Merced, California 95344, and
Institute of Chemistry, UMR6510, University of Rennes 1, France

Received: August 15, 2005; In Final Form: September 23, 2005

Resonance Raman and resonance hyper-Raman spectra and excitation profiles have been measured for a “push–pull” donor–acceptor substituted conjugated polyene bearing a julolidine donor group and a nitrophenyl acceptor group, in acetone at excitation wavelengths from 485 to 356 nm (two-photon wavelengths for the nonlinear spectra). These wavelengths span the strong visible to near-UV linear absorption spectrum, which appears to involve at least three different electronic transitions. The relative intensities of different vibrational bands vary considerably across the excitation spectrum, with the hyper-Raman spectra showing greater variation than the linear Raman. A previously derived theory of resonance hyper-Raman intensities is modified to include contributions from purely vibrational levels of the ground electronic state as intermediate states in the two-photon absorption process. These contributions are found to have only a slight effect on the hyper-Rayleigh intensities and profiles, but they significantly influence some of the hyper-Raman profiles. The absorption spectrum and the Raman, hyper-Rayleigh, and hyper-Raman excitation profiles are quantitatively simulated under the assumption that three excited electronic states contribute to the one- and two-photon absorption in this region. The transition centered near 400 nm is largely localized on the nitrophenyl group, while the transitions near 475 and 355 nm are more delocalized.

Introduction

Resonance Raman (RR) spectroscopy is an attractive method for deducing aspects of excited-state structure and dynamics in molecules that have diffuse absorption spectra.^{1–4} The vibrations that appear with high intensity in the spectrum are the same modes that would form vibronic progressions in the electronic spectrum if it were resolved. Quantitative simulation of the absorption spectrum and Raman excitation profiles with a self-consistent set of parameters can be used to obtain the geometry changes that occur upon electronic excitation and to partition the electronic line broadening into homogeneous and inhomogeneous contributions. Resonance Raman intensity analysis has been applied to probe the structure and dynamics of electronic transitions in a wide variety of molecules, including a number of conjugated organic molecules that are of interest for second-order nonlinear optical applications.^{5–10}

The resonance Raman intensity is proportional to the square of the product of one-photon absorption and one-photon emission transition dipole moments between the ground and resonant electronic states. It does not directly probe two-photon excitations except to the extent that they are also one-photon allowed. In view of the many applications of two-photon absorption in organic molecules such as two-photon-excited fluorescence microscopy,^{11–13} optical limiting,^{14–17} photorefractive materials,^{18–20} electrooptic modulators for telecommunications,^{21–24} 3D optical data storage,^{25,26} and microfabrication techniques,²⁷ there is a need for methods to better characterize such states. Resonance hyper-Raman spectroscopy

(RHR, Figure 1) can provide analogous information to linear resonance Raman for electronic transitions that are both one-photon and two-photon allowed, as are most of the transitions of polar, donor–acceptor substituted push–pull chromophores. When multiple electronic transitions overlap, generally all of them will contribute to both linear Raman and hyper-Raman enhancements but to different extents because of their different relative one-photon and two-photon transition strengths. Simultaneous analysis of both the linear and nonlinear spectra and excitation profiles allows the energies and structures of multiple, overlapping electronic transitions to be determined more accurately than does analysis of a single type of spectrum alone.

We previously presented RR and RHR spectra as a function of excitation wavelength for the donor–acceptor substituted polyene henceforth known as **3[5]** (see Figure 2 for the structure). When the excitation wavelength (or its second harmonic, in the hyper-Raman case) lies on the red side of the absorption maximum, the intensity patterns in the resonance Raman and hyper-Raman spectra are essentially identical.²⁸ As the resonant frequency is tuned toward the blue, into a region of broad absorption, certain vibrations become relatively much more intense in the RHR spectra than in the corresponding RR spectra.²⁹ This was interpreted qualitatively as resulting from more than one overlapping electronic transition having different excited-state geometries and different relative one- and two-photon absorption strengths and therefore contributing differently to the RR and RHR enhancements. More recently, we developed a quantitative theory of RHR intensities appropriate for large “push–pull” chromophores in solution and used it to model the RHR excitation profiles of a donor–acceptor substituted distyrylbenzene.³⁰ Here the excitation wavelengths used span two resolvable absorption bands, and while the intensity patterns in both the RR and RHR spectra change as

* Corresponding author phone: (209)724-4345; fax: (209)724-4356; e-mail: amkelley@ucmerced.edu.

[†] University of California, Merced.

[‡] University of Rennes 1.

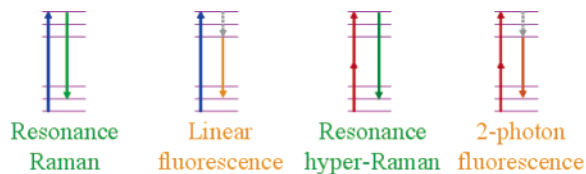


Figure 1. Schematic of resonance Raman and resonance hyper-Raman processes and their fluorescence analogues.

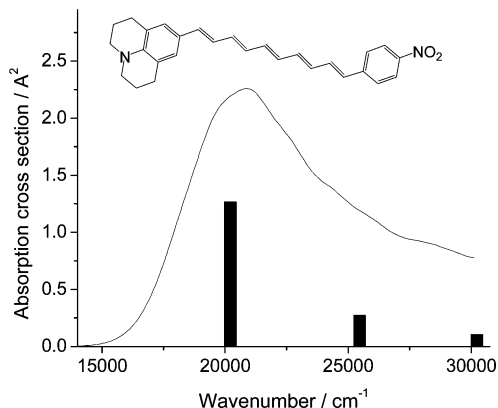


Figure 2. Linear absorption spectrum of **3[5]** in acetone. The bars show the positions and relative oscillator strengths calculated for the three lowest-energy substantially allowed transitions.

the excitation is tuned, the RR and RHR spectra remain similar to one another at all excitation wavelengths. We interpreted this result to mean that there are at least two electronic transitions having different excited-state geometries but comparable relative one- and two-photon transition strengths, so both contribute about equally to the RR and RHR enhancements.

Here we report quantitative measurements of the resonance Raman cross sections and resonance hyper-Rayleigh and hyper-Raman hyperpolarizabilities for **3[5]** in dilute acetone solution. We also present computational simulations of the linear absorption, hyper-Rayleigh, resonance Raman, and resonance hyper-Raman profiles using a model that assumes three resonant electronic states. The theory developed previously³⁰ is extended to include contributions from excited vibrational levels of the ground electronic state as intermediate states.³¹ It has been argued that these contributions should be considered in calculating two-photon absorption profiles, and they might be expected to play an equally or more important role in hyper-Raman scattering.

Theory

Our previous work on hyper-Raman scattering^{28–30} started from the following expression for the hyperpolarizability tensor associated with a $|0\rangle \rightarrow |f\rangle$ vibrational hyper-Raman transition when near two-photon resonance with a single electronic state e :

$$\beta_{ijk} = \sum_{s,v} \frac{\mu_{ge}^i \mu_{es}^j \mu_{sg}^k \langle f|v\rangle \langle v|0\rangle}{(\bar{\omega}_s - \omega)(\omega_{ev} - 2\omega - i\Gamma)} \quad (1)$$

This expression assumes that the sum over intermediate electronic states s excludes the ground state. It uses the Condon approximation to separate the dipole moment matrix elements into products of electronic transition dipole moments ($\mu_{ge}^i \mu_{es}^j \mu_{sg}^k$) and vibrational Franck–Condon factors ($\langle f|v\rangle \langle v|0\rangle$). Furthermore, all $g \rightarrow s$ transitions are assumed to be far from resonance with ω , so the quantity $\bar{\omega}_s - \omega$ is nearly

the same for all vibrational sublevels of s , allowing closure to be used to remove the sums over vibrational sublevels of s . A more general starting point is

$$\beta_{ijk} = \sum_{m,n} \frac{\langle f|\mu^i|m\rangle \langle m|\mu^j|n\rangle \langle n|\mu^k|g\rangle}{(\omega_{ng} - \omega)(\omega_{mg} - 2\omega - i\Gamma_{mg})} \quad (2)$$

where the state labels now refer to molecular (vibronic) states. Using the Born–Oppenheimer approximation to separate each molecular state into a product of electronic and vibrational states gives

$$\beta_{ijk} = \sum_{m,v} \frac{\langle f|g|\mu^i|m\rangle \langle v|\langle m|\mu^j|n\rangle \langle w|\langle n|\mu^k|g\rangle|0\rangle}{(\omega_{mw,g0} - \omega)(\omega_{nv,g0} - 2\omega - i\Gamma_{mv,g0})} \quad (3)$$

where g , m , and n label electronic states and $\{|v\rangle\}$ and $\{|w\rangle\}$ are vibrational sublevels of $|m\rangle$ and $|n\rangle$, respectively. If we further make the usual assumption that the fundamental frequency is far from resonance with any transition, we can set $(\omega_{mw,g0} - \omega) \approx (\bar{\omega}_{n,g} - \omega)$ and use closure to remove the summation over vibrational levels w , leaving

$$\beta_{ijk} = \sum_{m,n} \frac{\langle f|g|\mu^i|m\rangle \langle v|\langle m|\mu^j|n\rangle \langle n|\mu^k|g\rangle|0\rangle}{(\bar{\omega}_{n,g} - \omega)(\omega_{mv,g0} - 2\omega - i\Gamma_{mv,g0})} \quad (4)$$

The dipole matrix elements are then expanded in the usual manner as a Taylor series about the ground-state equilibrium geometry, e.g., $\langle n|\mu^k|g\rangle = \mu_{ng}^k(q_0) + \sum_l (\partial \mu_{ng}^k / \partial q_l)_0 q_l$ where the sum runs over all vibrational normal modes q_l . If we make the assumption that for strongly allowed electronic transitions the first term in the expansion should dominate, the vibronic matrix elements factor into products of purely electronic transition moments and vibrational overlaps, leading to eq 1. When the $(\partial \mu / \partial q)$ terms are retained, additional paths that involve purely vibrational transitions, in either the ground or the excited-state manifold, can contribute to the hyper-Rayleigh and hyper-Raman hyperpolarizabilities. Painelli has argued, using a two-state one-mode model for push–pull chromophores, that such transitions are important and lead to an overall blue-shift in the two-photon absorption spectrum relative to the linear absorption spectrum even if both processes terminate at the same, single two-photon-resonant electronic state.³¹

We therefore consider the additional terms in eq 4 that are linear in $(\partial \mu / \partial q)$. When $n = g$, the vibronic matrix element is the same as for a vibrational infrared transition, and the second term in the expansion of the electronic dipole matrix element in vibrational coordinates is the leading term. That is, $\langle w|\langle n|\mu^k|g\rangle|0\rangle$ becomes $\sum_l (\partial \mu_g^k / \partial q_l)_0 \langle w|q_l|0\rangle$. In the harmonic approximation this is nonzero only if $|w\rangle$ is the vibrational fundamental in mode q_1 , leading to $\langle w|\langle n|\mu^k|g\rangle|0\rangle = \sum_l (1/\sqrt{2})(\partial \mu_g^k / \partial q_l)_0$ for $|w\rangle = |1\rangle_l$ only. Inserting this result into eq 4, we obtain

$$\beta_{ijk} = \sum_l \frac{(\partial \mu_g^k / \partial q_l)}{\sqrt{2}(\omega_l - \omega)} \sum_{m,v} \mu_{gm}^i \mu_{gm}^j \frac{\langle f|v\rangle \langle v|1_l\rangle}{(\omega_{mv,g0} - 2\omega - i\Gamma_{mv,g0})} + \quad n \neq g \text{ term} \quad (5)$$

Here ω_l is the fundamental vibrational frequency of mode l , and the “ $n \neq g$ term” is the part that leads to eq 1. In our previous work,³⁰ the $n \neq g$ term was reformulated into a time-domain expression and specialized to the case of two electronic

states that are two-photon resonant or near-resonant. Performing the corresponding manipulations on the $n = g$ term of eq 5 and specializing to the case of a single tensor element as appropriate for **3[5]** (vide infra) leads to the following expression for the total two-photon-resonant hyperpolarizability:

$$\beta_{zzz} = \sum_{n=1}^N \left(\mu_{gn} \left\{ \frac{\Delta\mu_{ng}\mu_{ng}}{\bar{\omega}_n - \omega} + \sum_{m \neq n} \frac{\mu_{nm}\mu_{mg}}{\bar{\omega}_m - \omega} \right\} i \int_0^\infty dt \langle f|0(t) \rangle_n \times \right. \\ \left. \exp[i(2\omega - \omega_n)t - g_n(t)] + \sum_l \frac{i(\partial\mu_g/\partial q_l)}{\sqrt{2}(\omega_l - \omega)} \left| \mu_{gn} \right|^2 \int_0^\infty dt \langle f|1_l(t) \rangle_n \exp[i(2\omega - \omega_n)t - g_n(t)] \right) \quad (6)$$

Here N is the total number of two-photon-resonant or near-resonant electronic states, and we have suppressed the indices on the transition dipole directions, assuming that all transitions are polarized along the molecule-fixed z axis. The first term of eq 6 is the same as derived before, while the second term arises from the previously neglected path in which vibrational levels of the ground state act as intermediate states. The zero–zero frequency of the $g \rightarrow n$ transition is ω_n , $\bar{\omega}_n$ is the vibronically averaged transition frequency, $g_n(t)$ is the electronic line broadening function modeled here as a Brownian oscillator,^{32,33} and $\Delta\mu_{ng}$ is the permanent dipole moment difference between excited state n and the ground state. We define $|0(t)\rangle_n = \exp(-iH_{\text{vib},n}t/\hbar)|0\rangle$ where $H_{\text{vib},n}$ is the Hamiltonian for vibrational motion in excited state n , and analogously for the $v = 1$ initial vibrational state.

To estimate the importance of the vibrational paths in eq 6 (the second term) relative to the vibronic paths (first term), we need reasonable estimates for the dipole derivatives $\partial\mu/\partial q$. The numerators of the vibronic paths contain a product of either three electronic transition moments or two transition moments and the excited state to ground-state dipole moment difference, while the vibrational path depends on two electronic transition moments multiplied by the derivative of the ground-state dipole with respect to a normal coordinate. The theoretical expression for the intensity of an infrared absorption band is³⁴

$$A = \frac{N_A \pi}{3c^2} \left| \frac{\partial\mu}{\partial Q} \right|^2 \quad (7)$$

which has units of length per mol and is typically given in km mol⁻¹. N_A is Avogadro's number, c is the speed of light in cm s⁻¹, μ is the dipole moment in esu cm, and Q is the normal coordinate in g^{1/2} cm, which is related to the dimensionless normal coordinate in eqs 5 and 6 by $q = (\omega/\hbar)^{1/2}Q$.

Density functional calculations (vide infra) give the infrared intensities for the strongest modes in the 1000–1700 cm⁻¹ region as 1500–2500 km mol⁻¹. This translates, using eq 7, to $\partial\mu/\partial q$ values about an order of magnitude smaller than the electronic transition dipoles and dipole differences for similar molecules.³⁰ The denominators of the prefactors are similar in magnitude for both terms, as the fundamental frequency ω lies in the 10000–14000 cm⁻¹ range, while the electronic frequencies $\bar{\omega}_n$ are in the 20000–30000 cm⁻¹ range and the vibrational frequencies ω_l are 100–3000 cm⁻¹. Thus we conclude that the vibrational term should be small, but perhaps not negligible, relative to the vibronic term, and it should be considered in a general formulation of hyper-Raman intensities.

The above development considers only the contribution to the $n = g$ path from the non-Condon terms. More generally, the non-Condon (linear in $\partial\mu/\partial q$) terms also make an additional contribution to the $n \neq g$ paths;³¹ however, the parameters needed to evaluate this contribution do not reduce simply to any experimentally accessible quantity in the same way that the $n = g$ contribution reduces to an experimental IR intensity. We therefore omit the non-Condon contributions to the $n \neq g$ paths in the present analysis.

Finally, eq 6 for β , as well as eq 5 of ref 30, refer to the hyperpolarizability evaluated for specific values of the transition energies ω_n . For comparison with experiment, the hyperpolarizability must be averaged over an inhomogeneous distribution of these electronic energies, as is implicit in eq 1 of ref 30. The inhomogeneous averaging is performed at the level of $|\beta|^2$, not β , as it accounts for the contributions of different molecules to the total, incoherent scattering intensity. In both ref 30 and here, we treat the inhomogeneous broadening as a Gaussian distribution of electronic zero–zero energies and assume that a given local environment shifts all electronic transition energies by the same amount. In reality the shifts for different states may be different in magnitude and are not necessarily fully correlated,³⁵ but identical distributions are assumed here in the absence of other information.

Experimental Methods

Resonance Raman and resonance hyper-Raman spectra were obtained using the instrumentation and methods described previously.^{29,30} Hyper-Rayleigh intensities were measured from 1014 to 721 nm and hyper-Raman and resonance Raman spectra were obtained from 970 to 713 nm and 485 to 356 nm, respectively, using excitation from the fundamental and second harmonic of a picosecond mode-locked Spectra-Physics Tsunami Ti:sapphire laser. Resonance Raman spectra were also obtained using excitation wavelengths between 514.5 and 476.5 nm from a Coherent Innova 90C-5 argon-ion laser as well as 532 nm excitation from the Millennia Nd pump laser. All spectra were corrected for the wavelength dependence of the spectrograph throughput and detector sensitivity and for reabsorption of the scattered light. Integrated peak areas were determined from the intensity-corrected spectra by fitting regions of the spectra to sums of Gaussian–Lorentzian peaks plus a linear baseline following subtraction of a low-order polynomial to remove background fluorescence. Resonance Raman cross-sections were measured relative to those of the acetone solvent as an internal standard.³⁰ The hyper-Raman intensities were measured relative to the hyper-Rayleigh intensities, and the latter were placed on an absolute hyperpolarizability scale by reference to the hyper-Rayleigh scattering from liquid acetonitrile as an external standard as described previously.³⁰ The synthesis of **3[5]** was described in ref 36. Samples were prepared in spectroscopic grade acetone at concentrations of 0.10–0.18 mM for the resonance Raman and hyper-Raman experiments and 0.01–0.02 mM for the hyper-Rayleigh intensity measurements. Absorption spectra were measured on a Hitachi U-3010 UV/vis spectrophotometer.

It was found that even with an unamplified picosecond mode-locked laser as a light source, under our tight laser focusing conditions the hyper-Rayleigh signal exhibited a subquadratic dependence on laser power at certain wavelengths owing to saturation of the two-photon absorption. Neutral density filters were used to attenuate the incident laser as necessary to reach a region where the hyper-Raman signal exhibited the expected quadratic dependence on laser power.

The infrared spectrum of **3**[**5**] in perdeuterated dimethyl sulfoxide (DMSO- d_6 , Aldrich, 99.96%) was obtained on a Bruker IFS 66 series FT-IR spectrometer at a spectral resolution of 4 cm^{-1} . The spectrum was recorded in transmission mode using a Harrick Scientific DLC 2 demountable liquid sample IR cell equipped with ZnSe windows. Limited solubility necessitated a rather low concentration (1 mM) and a correspondingly long path length (950 μm). At this path length, d_6 -DMSO has adequate transmission to allow measurement of bands in the 1140–1700 cm^{-1} region, encompassing most but not all of the detected resonance Raman and hyper-Raman bands. The experimental IR absorption intensity corresponding to the theoretical expression in eq 7 is³⁷

$$A = \frac{1}{nL} \int_{\text{band}} \ln\left(\frac{I_0}{I}\right) d\nu \quad (8)$$

where n is the molar concentration of chromophore, L is the path length, I/I_0 is the transmittance, ν is the wavenumber, and the IR intensity is integrated over the vibrational band of interest. The experimental IR transmission spectra were converted to absorbance, baseline corrected, and integrated in the same manner as the Raman bands.

Computational Methods

The absorption and linear resonance Raman spectra were simulated via the time-domain wave packet method as described in previous publications,^{35,38} generalized to three rather than two resonant electronic transitions. Each Raman-active mode was treated as a harmonic oscillator characterized by its ground-state frequency and displacements Δ , in dimensionless normal coordinates, between the potential minima in the ground state and each excited state. The electronic line width was partitioned into static inhomogeneous broadening, modeled as a Gaussian distribution of electronic zero–zero energies, and homogeneous broadening, described by coupling of the electronic transition to an overdamped Brownian oscillator representing the solvent degrees of freedom. All three resonant electronic transitions were assumed to have parallel transition dipoles based on ZINDO calculations (vide infra) which indicate that the three lowest allowed transitions have transition dipole directions that differ by no more than 16°. The resonance Raman and hyper-Raman depolarization ratios are also consistent with this assumption.³⁹ The other parameters required to model the absorption spectra and resonance Raman profiles are the zero–zero energies and transition moments of the three electronic states. The parameters were adjusted to obtain the best simultaneous fit to the absorption spectrum and the absolute resonance Raman cross sections at all measured wavelengths. Neither the absorption spectra nor the resonance Raman and hyper-Raman profiles could be fit adequately by using fewer than three electronic transitions.

Calculations of the ground-state equilibrium geometry, vibrational frequencies, and infrared intensities were performed using density functional theory with the B3LYP hybrid density functional and the 6-31G** basis set as implemented in the Gaussian 98 package.⁴⁰ To keep the computations tractable, the julolidine donor group was replaced by dimethylaminophenyl for these calculations. The electronic excitation energies, transition moments, and oscillator strengths were calculated using the ZINDO method as implemented in Gaussian 98. The excited-state calculations included configuration interaction among all singly excited configurations formed from the 41 lowest occupied and 49 highest unoccupied molecular orbitals.

The parameters derived from the resonance Raman and absorption spectral modeling were then transferred to simulations of the hyper-Rayleigh and hyper-Raman hyperpolarizability profiles via eq 6 with the assumption that β_{zzz} is the only nonvanishing tensor element. Equations 7 and 8 were used to calculate the vibrational dipole moment derivatives ($\partial\mu/\partial q$) for each IR band that corresponds to an observed Raman band. Several of the Raman transitions did not exhibit detectable IR intensity, and $(\partial\mu/\partial q)$ was set to zero for these modes as well as for the two (1008 and 1108 cm^{-1}) that fall in spectral regions obscured by solvent absorption. The transition dipole moments between excited electronic states were fixed to the same approximate ratio as obtained from the ZINDO calculations: $\mu_{13} = 2\mu_{12}$ and $\mu_{23} = 0$. The permanent dipole moment differences, $\Delta\mu_{ng}$, as well as the magnitude of the μ_{13} transition dipole, were then chosen to best fit the hyper-Rayleigh profiles. Finally, all of the parameters from the absorption and resonance Raman simulations were iteratively adjusted to improve the fit to all four pieces of data (linear absorption, resonance Raman, hyper-Raman, and hyper-Rayleigh) simultaneously.

The hyper-Rayleigh and hyper-Raman calculations involve several molecular parameters that are real quantities but can be either positive or negative: the transition dipole moments μ_{ng} and μ_{mn} , the permanent dipole moment changes $\Delta\mu_{ng}$, the excited-state displacements Δ , and the dipole derivatives $\partial\mu/\partial q$. The signs of these quantities determine whether the contributions from the vibronic and vibrational paths and the contributions from different electronic states add constructively or destructively toward the total β , whose absolute square determines the experimentally observed intensities. The linear absorption oscillator strengths and the IR intensities provide the absolute magnitudes of μ_{ng} and $\partial\mu/\partial q$, respectively, but not their signs. The molecular geometry chosen places the NO_2 group along the positive z axis, making the permanent dipole moments negative; since the excited states are expected to have more charge separation than the ground state (larger negative dipole moment), the $\Delta\mu_{ng}$ should be negative quantities. The transition dipoles depend on the signs of the wave functions, and any given transition moment can be reversed by changing the sign of one of the wave functions involved; however, the relationships between transition moments involving multiple states cannot be altered arbitrarily. With appropriate choices of wave function sign all of the transition dipoles can be made positive according to the ZINDO results, and this assumption was maintained throughout. The signs of the Δ depend on the choice of phase of the wave function which is arbitrary, but the relative signs of the Δ in different electronic states are not arbitrary. We have taken the signs to be positive for all modes in all three states under the assumption that all three transitions are essentially $\pi \rightarrow \pi^*$ excitations, which should be reasonable at least for the stronger Raman lines. The signs of the $\partial\mu/\partial q$ were left as adjustable parameters in the fitting procedure, and negative values were found to give the best results.

Results

Figure 2 shows the linear absorption spectrum of **3**[**5**] in acetone and gives its molecular structure. The spectra are superimposable over the concentration range from 0.12 to 0.01 mM, indicating that aggregation is not significant. The spectrum shows a clear maximum at about 480 nm and two poorly defined shoulders near 400 and 355 nm. ZINDO calculations also predict three one-photon allowed transitions in this general region: the $0 \rightarrow 2$ transition at 495 nm with a one-photon oscillator strength of 2.52, $0 \rightarrow 4$ at 393 nm with $f = 0.55$, and $0 \rightarrow 5$ at 331 nm

TABLE 1: Experimental and Calculated Vibrations of 3[5]

Raman freq/cm ⁻¹ ^a	IR freq/cm ⁻¹ ^a	calc freq/cm ⁻¹ ^b	calc IR intensity/km mol ⁻¹ ^b	calc mode description ^b
1008 (vw)	^c	1026	10	trigonal phenyl def
1108 (w)	^c	1130	683	ring C–NO ₂ str
1141 (m)	1140 (m)	1177	25	chain C–C in-phase str
		1183	1595	chain CH in-phase rock
1210 (w)	1206 (m)	1246	261	chain and ring CH rocks
1290 (w)	1283 (w)	{ 1323 1326 }	{ 130 132 }	chain CH rocks
1313 (w)	1313 (s)	1342	285	chain CH rocks
1337 (m)	1334 (s)	1381	2565	sym. NO ₂ str
1552 (s)	1543 (m)	1599	1520	in-phase chain C=C str
1585 (w), 1616 (vw)	1596 (m)	{ 1644 1664 1669 }	{ 9 272 203 }	phenyl quinoidal str, out-of-phase C=C str

^a Qualitative relative intensities in parentheses. Only lines with significant Raman intensity are listed. The IR spectrum also has a strong line at 1508 cm⁻¹, and a number of weaker lines that do not correspond to observed Raman transitions. ^b From DFT calculations. ^c Not observed because of solvent absorbance.

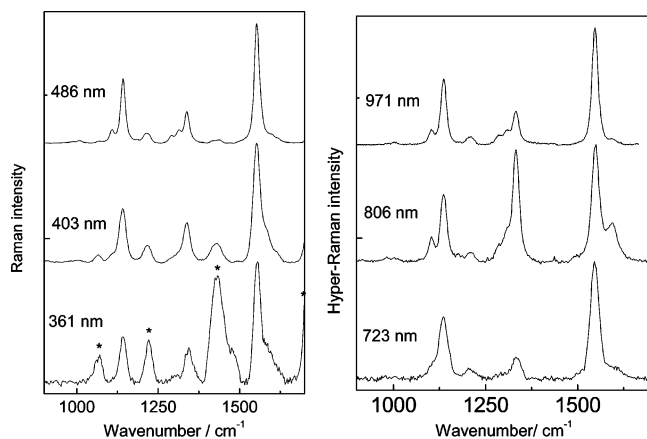


Figure 3. Left: Resonance Raman spectra of 3[5] in acetone at the indicated excitation wavelengths. Solvent bands are marked with asterisks, shown only in the 361 nm spectrum. Spectra are arbitrarily scaled and offset vertically. Right: The corresponding resonance hyper-Raman spectra.

with $f = 0.21$. These are the only transitions calculated to the red of 240 nm with oscillator strengths exceeding 0.05. The reasonable agreement between experimental and calculated linear absorption spectra provides justification for the assumption of three electronic transitions in the spectroscopic modeling.

Figure 3 shows representative resonance Raman and resonance hyper-Raman spectra at several excitation wavelengths spanning the region investigated. Table 1 summarizes the experimental Raman and IR frequencies along with the frequencies, normal mode descriptions, and infrared intensities obtained from the density functional calculations. In some cases there is considerable ambiguity about the assignment of an experimental frequency to a particular calculated normal mode. The correspondence between IR and Raman frequencies is questionable in some cases, reflecting some combination of solvent-dependent vibrational frequencies, incomplete resolution of overlapping transitions, and, perhaps, actual differences in the normal modes giving rise to the Raman and IR transitions.

Both the resonance Raman and hyper-Raman spectra are dominated by strong lines at 1552, 1337, and 1141 cm⁻¹. There are also weaker lines at 1008, 1108, and 1210 cm⁻¹, at least two weak lines in the 1285–1315 cm⁻¹ region, and at least two lines in the 1585–1620 cm⁻¹ range. In the resonance Raman spectra the three strongest lines have the same intensity ordering (1552 > 1141 > 1337) at all excitation wavelengths examined, although there are some variations in the relative

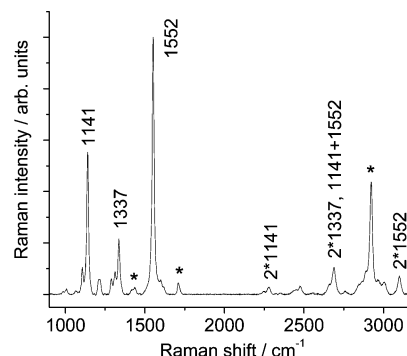


Figure 4. Resonance Raman spectrum of 3[5] in acetone at 514.5 nm excitation. A fluorescence background has been subtracted. Solvent bands are marked with asterisks, and major fundamentals, overtones, and combination bands are labeled.

intensities and the shoulder on the high-frequency side of the 1552 cm⁻¹ line clearly gains intensity as the excitation is tuned toward the blue. The hyper-Raman spectra are nearly identical to the resonance Raman spectra when excited near or to the red of the absorption maximum as reported previously,^{28,29} but they show a much stronger variation with excitation frequency. At two-photon wavelengths near 400 nm, the 1337 and 1585 cm⁻¹ lines exhibit large increases in intensity relative to the 1552 and 1141 cm⁻¹ lines, but farther to the blue, near 360 nm, the intensity pattern again becomes similar to that observed in the red. These wavelength-dependent intensity patterns have much in common with those of the push–pull substituted distyrylbenzene chromophore we reported recently,³⁰ which also contains a nitrophenyl group; however, the differences between the resonance Raman and hyper-Raman spectra are much greater in 3[5] than in that molecule.

Figure 4 shows a more complete resonance Raman spectrum, including the overtone and combination band region, obtained with 514.5 nm excitation. The overtone intensities were used mainly for establishing the absolute magnitudes of the displacements (Δ) in the lowest-energy excited state.^{2,41} While the relative Δ values for different modes are well defined by their relative resonance Raman intensities, a wide range of Δ_{max} values (coupled with adjustments to the homogeneous and inhomogeneous line widths) can fit the fundamental Raman intensities and the absorption spectrum about equally well, and the additional information provided by the overtone intensities is needed to establish the absolute scaling of the displacements. (The hyper-Raman to hyper-Rayleigh ratio can provide equivalent information if a single electronic transition dominates the

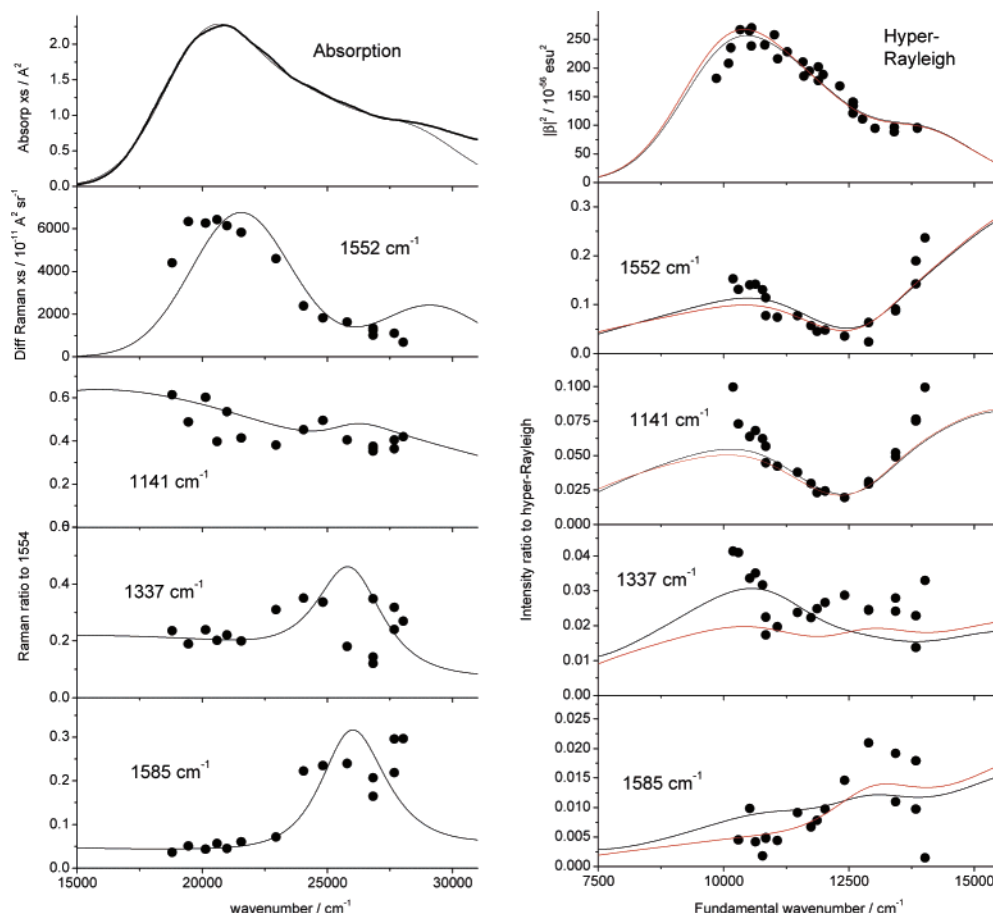


Figure 5. Comparison of experimental (points or thick line) and simulated (thin lines) profiles for **3[5]** in acetone. Linear absorption spectrum, hyper-Rayleigh profile, and 1552 cm^{-1} Raman profile are displayed as absolute intensities; other Raman profiles are plotted relative to 1552 cm^{-1} intensity, and hyper-Raman profiles are plotted relative to hyper-Rayleigh intensity. Black curves are generated from parameters of Table 2. Red curves use same parameters but with all $d\mu/dq$ set to zero.

nonlinear scattering.) The overtones of the 1141 and 1552 cm^{-1} lines are clearly observed, as is a band that contains the overlapping 1337 cm^{-1} overtone and $1141+1552\text{ cm}^{-1}$ combination band.

The spectroscopic modeling was carried out by first fitting the longest-wavelength resonance Raman data ($532\text{--}460\text{ nm}$), including the intensities of the 1141 and 1552 cm^{-1} overtones, and the low-energy side of the absorption spectrum to a single electronic transition. This transition is significantly stronger than the other two, and it dominates the Raman and hyper-Raman intensities throughout most of the excitation region explored. These parameters were then fixed, the two other transitions were added, and their parameters were adjusted to best reproduce the full Raman profiles and the absorption spectrum in the $12000\text{--}30000\text{ cm}^{-1}$ region. Finally, the hyper-Rayleigh and hyper-Raman profiles were added, and all parameters were readjusted to obtain a best simultaneous fit to all of the data.

Figure 5 shows the calculated fits to the experimental absorption spectrum, the hyper-Rayleigh excitation profile, and the relative resonance Raman and resonance hyper-Raman excitation profiles for four of the principal vibrational modes. Table 2 gives the best-fit parameters used in our simulations of all of the spectroscopic observables.

The vibrational parameters for the lowest-energy transition are quite well defined by the fitting procedure, as the red edge of the absorption spectrum and the Raman and hyper-Raman intensities excited in this region are determined almost entirely by the properties of the lowest-energy, most strongly allowed transition. The vibrational parameters for the second and third

transitions are far less well defined. However, the general features of the model—particularly, the dominance of the 1552 and 1141 cm^{-1} modes in the first transition and of the 1337 and 1585 cm^{-1} modes in the second transition—appear quite robust. The parameters for the third state are the least well defined because it is the weakest of the three transitions and the most strongly overlapped by the other two. However, this transition must be included in order to reproduce the “U-shaped” hyper-Raman profiles for many of the transitions (see the 1141 and 1552 cm^{-1} hyper-Raman profiles in Figure 5) as well as to obtain a reasonable fit to the region of the absorption spectrum with which our excitation wavelengths are resonant. The electronic parameters associated only with the two-photon transitions—the $\Delta\mu$ and the excited state to excited-state transition dipoles—are not very well defined, and there are a number of different combinations that fit the hyper-Rayleigh and hyper-Raman spectra about equally well. Also note that eliminating the vibrational path in the two-photon excitation step by setting all of the $d\mu/dq$ to zero has a barely discernible effect on the hyper-Rayleigh profile (see upper right-hand panel of Figure 5) but larger effects on the hyper-Raman profiles for some of the modes.

Discussion

Previous treatments of the theory of resonance hyper-Raman scattering^{42,43} did not explicitly consider the “vibrational” paths that give rise to the second term in eq 6. In contrast, there has been much discussion of the importance of these paths in

TABLE 2: Parameters Used in Simulation of Absorption Spectrum and Resonance Raman, Hyper-Rayleigh, and Hyper-Raman Intensities

vib freq/cm ⁻¹	$\partial\mu/\partial q^a/\text{e}\text{\AA}$	Δ (state 1) ^b	Δ (state 2) ^b	Δ (state 3) ^b
1008	0	0.06	0.03	0.02
1108	0	0.14	0.04	0.07
1141	-0.056	0.32	0.08	0.32
1210	-0.039	0.11	0.03	0.11
1290	-0.026	0.10	0.01	0.01
1313	-0.120	0.09	0.04	0.09
1337	-0.117	0.18	0.14	0.14
1552	-0.088	0.38	0.04	0.45
1585	-0.068	0.08	0.12	0.11
1616	0	0.03	0.05	0.03
<hr/>				
		state 1	state 2	state 3
electronic zero–zero energy/cm ⁻¹		19200	23800	27200
solvent reorg energy ^c /cm ⁻¹		880	450	760
grd \rightarrow exc state transition dipole/e \AA		2.75	1.60	1.38
exc – grd state permanent dipole difference/e \AA		-2.75	0.	-2.7
electronic inhomog width (Gaussian std dev)/cm ⁻¹			1800	
temperature/K			298	
transition dipoles between exc states/e \AA			$\mu_{12} = 1.0, \mu_{13} = 2.0, \mu_{23} = 0$	

^a From experimental IR intensities in d₆-DMSO solution. ^b Displacement along normal mode between potential minima of excited and ground states in dimensionless normal coordinates. ^c Based on overdamped Brownian oscillator model for the solvent dynamics with $\kappa = 0.1$ (ref 32).

evaluating nonresonant hyperpolarizabilities.^{44–46} While the vibrational contributions are sometimes claimed to be large or even dominant over the purely electronic ones, such statements often refer to hyperpolarizabilities calculated in the static (zero-frequency) limit. Mukamel and co-workers determined that the vibrational paths make only a minor contribution to the hyperpolarizability evaluated at intermediate frequencies, i.e. above vibrational resonances and below electronic ones.⁴⁷ Kuzyk et al. concluded that all vibrational effects should have only modest ($\sim 5\%$) effects on even the static hyperpolarizabilities of push–pull molecules.⁴⁸ On the other hand, Painelli and co-workers argue that the vibrational contributions must be included in order to obtain the correct two-photon absorption profiles for push–pull molecules,³¹ and Bishop and co-workers also stress the importance of these contributions to two-photon absorption.⁴⁹ In this work, the IR absorption strengths that determine the importance of the vibrational paths are measured directly. The strongest IR band (the 1337 cm⁻¹ NO₂ stretch) has an experimental intensity in solution of 530 km/mol, about five times smaller than predicted by the DFT calculation; the discrepancy may not be surprising given that the calculations were performed in the absence of solvent and for a molecule lacking the full julolidine ring. In this molecule the vibrational paths do not make an important contribution to the resonant hyper-Rayleigh profile, but they do have a more substantial effect on the hyper-Raman excitation profiles for modes that have large IR intensities.

We are aware of no previous measurements of resonant hyperpolarizabilities for this molecule. A previous determination of the off-resonance hyperpolarizability from EFISH measurements at 1907 nm gave $\beta = 530 \times 10^{-30}$ esu, which extrapolates using the standard two-level model to $\beta(0) = 360 \times 10^{-30}$ esu.³⁶ These values appear high relative to our maximum resonant value of about 1600×10^{-30} esu. However, we obtained a similar peak resonant hyperpolarizability of about 1200×10^{-30} esu for the donor–acceptor substituted distyrylbenzene that was the subject of our previous quantitative hyper-Rayleigh study.³⁰ Note that eq 6 is derived under the assumption of electronic two-photon resonance or near-resonance and lacks the electronically nonresonant terms,^{9,50} so it should not be expected to give correct nonresonant β values. As we have discussed previously,³⁰ there are often large discrepancies between the absolute hyper-

polarizabilities reported for the same chromophore or the same solvent by different groups, and our choice of Shelton's β value for acetonitrile⁵¹ as a standard may result in systematically lower hyperpolarizabilities than obtained by other workers using different intensity standards. There is a real need for careful, primary determinations of hyper-Rayleigh scattering intensities as a function of wavelength for solvents that can be used as hyperpolarizability standards, although such measurements are likely to be considerably more difficult than the corresponding determinations for ordinary Raman scattering.^{52–57}

The best-fit vibrational parameters for all three states shown in Table 2 are notable for their extremely small displacements (Δ), corresponding to a total vibrational reorganization energy of 235 cm⁻¹ for the strongest, lowest-energy transition. Vibrational reorganization energies for related push–pull chromophores are typically larger than this by factors of 1.5 to 5.^{7–9} However, small displacements were required to fit the general shapes of the resonance Raman and hyper-Raman excitation profiles as well as the resonance Raman overtone intensities. At excitation wavelengths between 476.5 and 532 nm (18796–20987 cm⁻¹), just slightly to the red of the first absorption maximum, the 1141 and 1552 cm⁻¹ overtones are only about 5–6% as intense as the corresponding fundamentals. These overtone intensities are reproduced well by the calculations using the small displacements, whereas increasing the displacements by more than about 30% clearly overcalculates the overtone intensities even when the other parameters are adjusted to obtain the correct fundamental intensities at the same excitation frequencies. Furthermore, the second transition must have even smaller displacements in the 1141 and 1552 cm⁻¹ modes in order to reproduce the pronounced minimum near 12500 cm⁻¹ in the hyper-Raman to hyper-Rayleigh intensity ratio profiles for these modes. Thus, while we would have considered such weak electron-vibration coupling unlikely for this molecule, we have been unable to simulate even the general features of the linear and nonlinear spectroscopic data using significantly larger couplings. It should be noted that we did not vary the relative signs of the displacements in the different excited states as it was felt that this would make the fits too poorly constrained. The ZINDO calculations predict that all three transitions are predominantly $\pi \rightarrow \pi^*$ in character, indicating that displacements of the same sign are most probable. However, since the various

π and π^* orbitals that contribute to the transitions have different nodal patterns (e.g. HOMO and HOMO-1 are different, as are LUMO and LUMO+1), a given normal mode could have displacements of different sign in different excited states, further complicating the analysis.

The most notable feature of Figure 3 is a large increase in the relative intensities of the 1337 and 1585 cm^{-1} lines in the hyper-Raman spectra at intermediate excitation wavelengths (near 800 nm). These apparent intensity increases are primarily a result of *decreases* in the intensities of the other strong lines at these excitation wavelengths, as evidenced by the minima in the experimental hyper-Raman/hyper-Rayleigh intensity ratios for the 1141 and 1552 cm^{-1} lines in Figure 5. In contrast, the hyper-Raman/hyper-Rayleigh intensity ratios for the 1337 and 1585 cm^{-1} lines are more nearly constant as a function of excitation wavelength. These results can be understood qualitatively by inspecting the Δ parameters for these modes in the three excited states (Table 2). The 1141 and 1552 cm^{-1} modes as well as most of the other modes have much smaller displacements in the second excited state than in the first and third states. This gives rise to the minimum in the hyper-Raman intensity (relative to the hyper-Rayleigh) at excitation wavelengths near 800 nm. The 1337 and 1585 cm^{-1} modes, in contrast, have similar displacements in all three states, giving rise to the flatter relative excitation profiles shown in Figure 5.

The above analysis, however, does not explain the different intensity patterns in the resonance Raman and hyper-Raman spectra, both of which depend on the same three excited states. The contribution of each excited state to the total resonance Raman or hyper-Raman amplitude is given by the product of a time integral, which is the same for hyper-Raman and resonance Raman at the same two-photon energy, and a prefactor, which is different for hyper-Raman and resonance Raman. For resonance Raman, the prefactor for each state is simply proportional to the square of its transition dipole moment, $|\mu_{gn}|^2$. This quantity is always positive, and it is about three times larger for state 1 than for either of the other two excited states. The contribution of a given excited state to the hyper-Raman is more complicated. If we neglect the $d\mu/dq$ terms in eq 6, it depends on the quantity

$$\mu_{gn} \left\{ \frac{\Delta\mu_{ng}\mu_{ng}}{\bar{\omega}_n - \omega} + \sum_{m \neq n} \frac{\mu_{nm}\mu_{mg}}{\bar{\omega}_m - \omega} \right\} \quad (9)$$

and if we ignore the denominators, which are all nonresonant, and specialize to the case of three excited states, the contribution of state n becomes $\mu_{gn}\{\Delta\mu_{ng}\mu_{ng} + \mu_{nm}\mu_{mg} + \mu_{nm'}\mu_{m'g}\}$ where m and m' represent the other two excited states. When we evaluate this collection of dipole and transition moments from the parameters of Table 2, we find that the prefactor for state 1 is of opposite sign and about twice as large as that for state 2, while state 3 has the same sign as state 2 and is another factor of 2 smaller. Because the time integrals are complex-valued quantities that have a complicated dependence on the excitation wavelength, arguments based on the signs of the prefactors cannot be simply interpreted. However, the net result is that, as a consequence of the magnitudes and relative signs of the transition moments and permanent dipole moments in this model, the first excited state makes a much more dominant contribution to the resonance Raman amplitude than to the hyper-Raman amplitude, thereby allowing the latter spectra to reveal more clearly the properties of the weaker electronic states.

In this molecule as well as most other push–pull chromophores we have examined^{28–30,58} the resonance Raman and

resonance hyper-Raman spectra are nearly identical when excited on the low-energy side of the first absorption maximum. We argued previously that this is expected when there is a single resonant excited electronic state that is both one- and two-photon allowed. The more complete analysis presented here suggests that the RR and RHR spectral patterns may be different even if a single electronic state dominates both processes because the vibrational paths [second term in eq 6] make an additional contribution to the RHR process. However, our quantitative analysis of **3**[5] indicates that the vibrational paths make a fairly small contribution to the total RHR intensity, and, in fact, the similarity of the RR and RHR spectra in the region of a single electronic resonance supports the relatively small importance of the vibrational paths.

We believe that this, and our previous work on a donor–acceptor substituted distyrylbenzene,³⁰ constitute the first published attempts to quantitatively simulate resonance hyper-Raman profiles for any molecule in liquid solution. The molecules studied possess multiple overlapping electronic transitions that contribute to both the linear and the nonlinear spectroscopies. These are precisely the types of molecules for which the hyper-Raman spectra are likely to be both strong and informative. However, purely empirical simulation of the spectra as reported here, and to a lesser extent in ref 30, is hindered by the large number of parameters and the resulting uncertainties in the uniqueness of the spectroscopic model. High-level electronic structure calculations would be helpful for guidance, at least, in the empirical modeling of such spectra. Since resonance Raman and hyper-Raman spectra of large molecules in solution are determined mainly by “short-time” nuclear dynamics,^{2,3,41,59} it is not necessary to calculate the equilibrium geometries and vibrational frequencies of the excited electronic states; the ground-state geometry, vibrational frequencies and normal modes, excited-state energies and one- and two-photon transition strengths, and the derivatives of the excited-state potential surfaces at the ground-state equilibrium geometry would provide most of the spectroscopically relevant information. Initial simulations of the spectra could be carried out using the parameters obtained from electronic structure theory, and those parameters then modified only as necessary to match the experimental data. Alternatively, different approaches to carrying out the electronic structure calculations could be evaluated by using each to calculate the linear and nonlinear vibrational spectra.

Acknowledgment. This work was supported by NSF grant CHE-0342816. We thank Prof. Sam Traina for his assistance in obtaining the IR spectrum and Prof. Anna Painelli for bringing to our attention the possible importance of vibrational paths in the hyper-Raman intensity.

References and Notes

- (1) Kelley, A. M. *J. Phys. Chem. A* **1999**, *103*, 6891.
- (2) Myers, A. B. In *Laser Techniques in Chemistry*; Myers, A. B., Rizzo, T. R., Eds.; Wiley: New York, 1995; p 325.
- (3) Myers, A. B. *Acc. Chem. Res.* **1997**, *30*, 519.
- (4) Myers, A. B. *J. Raman Spectrosc.* **1997**, *28*, 389.
- (5) Leng, W.; Wang, C. H.; Asato, A. E.; Kelley, A. M. *J. Phys. Chem. A* **2002**, *106*, 9479.
- (6) Moran, A. M.; Bartholomew, G. P.; Bazan, G. C.; Kelley, A. M. *J. Phys. Chem. A* **2002**, *106*, 4928.
- (7) Moran, A. M.; Blanchard-Desce, M.; Kelley, A. M. *Chem. Phys. Lett.* **2002**, *358*, 320.
- (8) Moran, A. M.; Delbecq, C.; Kelley, A. M. *J. Phys. Chem. A* **2001**, *105*, 10208.
- (9) Moran, A. M.; Egolf, D. S.; Blanchard-Desce, M.; Kelley, A. M. *J. Chem. Phys.* **2002**, *116*, 2542.
- (10) Moran, A. M.; Kelley, A. M. *J. Chem. Phys.* **2001**, *115*, 912.

- (11) So, P. T. C.; Dong, C. Y.; Masters, B. R.; Berland, K. M. *Ann. Rev. Biomed. Eng.* **2000**, 2, 399.
- (12) Williams, R. M.; Zipfel, W. R.; Webb, W. W. *Curr. Opin. Chem. Biol.* **2001**, 5, 603.
- (13) Xu, C.; Zipfel, W.; Shear, J. B.; Williams, R. M.; Webb, W. W. *Proc. Natl. Acad. Sci. U.S.A.* **1996**, 93, 10763.
- (14) Ehrlich, J. E.; Wu, X. L.; Lee, I. Y. S.; Hu, Z. Y.; Rockel, H.; Marder, S. R.; Perry, J. W. *Opt. Lett.* **1997**, 22, 1843.
- (15) He, G. S.; Xu, G. C.; Prasad, P. N.; Reinhardt, B. A.; Bhatt, J. C.; McKellar, R.; Dillard, A. G. *Opt. Lett.* **1995**, 20, 435.
- (16) Mongin, O.; Charlot, M.; Katan, C.; Porrès, L.; Parent, M.; Pons, T.; Mertz, J.; Blanchard-Desce, M. *Proc. SPIE* **2004**, 5516.
- (17) Silly, M. G.; Porrès, L.; Mongin, O.; Chollet, P.-A.; Blanchard-Desce, M. *Chem. Phys. Lett.* **2003**, 379, 74.
- (18) Barzoukas, M.; Blanchard-Desce, M. *J. Chem. Phys.* **2000**, 112, 2036.
- (19) Kippelen, B.; Sandalphon; Meerholz, K.; Peyghambarian, N. *Appl. Phys. Lett.* **1996**, 68, 1748.
- (20) Würthner, F.; Wortmann, R.; Meerholz, K. *ChemPhysChem* **2002**, 3, 17.
- (21) Lee, M.; Katz, H. E.; Erben, C.; Gill, D. M.; Gopalan, P.; Heber, J. D.; McGee, D. J. *Science* **2002**, 298, 1401.
- (22) Robinson, B. H.; Dalton, L. R.; Harper, A. W.; Ren, A.; Wang, F.; Zhang, C.; Todorova, G.; Lee, M.; Aniszfeld, R.; Garner, S.; Chen, A.; Steier, W. H.; Houbrecht, S.; Persoons, A.; Ledoux, I.; Zyss, J.; Jen, A. K. Y. *Chem. Phys.* **1999**, 245, 35.
- (23) Shi, Y.; Zhang, C.; Zhang, H.; Bechtel, J. H.; Dalton, L. R.; Robinson, B. H.; Steier, W. H. *Science* **2000**, 288, 119.
- (24) Thayumanavan, S.; Mendez, J.; Marder, S. R. *J. Org. Chem.* **1999**, 64, 4289.
- (25) Dvornikov, A. S.; Liang, Y.; Cruse, C. S.; Rentzepis, P. M. *J. Phys. Chem. B* **2004**, 108, 8652.
- (26) Strickler, J. H.; Webb, W. W. *Opt. Lett.* **1991**, 16, 1780.
- (27) Zhou, W.; Kuebler, S. M.; Braun, K. L.; Yu, T.; Cammack, J. K.; Ober, C. K.; Perry, J. W.; Marder, S. R. *Science* **2002**, 296, 1106.
- (28) Kelley, A. M.; Leng, W.; Blanchard-Desce, M. *J. Am. Chem. Soc.* **2003**, 125, 10520.
- (29) Shoute, L. C. T.; Blanchard-Desce, M.; Kelley, A. M. *J. Chem. Phys.* **2004**, 121, 7045.
- (30) Shoute, L. C. T.; Bartholomew, G. P.; Bazan, G. C.; Kelley, A. M. *J. Chem. Phys.* **2005**, 122, 184508.
- (31) Painelli, A.; Del Frio, L.; Terenziani, F. *Chem. Phys. Lett.* **2001**, 346, 470.
- (32) Li, B.; Johnson, A. E.; Mukamel, S.; Myers, A. B. *J. Am. Chem. Soc.* **1994**, 116, 11039.
- (33) Mukamel, S. *Principles of Nonlinear Optical Spectroscopy*; Oxford University Press: New York, 1995.
- (34) Darling, C. L.; Schlegel, H. B. *J. Phys. Chem.* **1994**, 98, 5855.
- (35) Waterland, M. R.; Kelley, A. M. *J. Chem. Phys.* **2000**, 113, 6760.
- (36) Blanchard-Desce, M.; Alain, V.; Midrier, L.; Wortmann, R.; Lebus, S.; Glania, C.; Kramer, P.; Fort, A.; Muller, J.; Barzoukas, M. *J. Photochem. Photobiol. A* **1997**, 105, 115.
- (37) Person, W. B.; Rudys, S. K.; Newton, J. H. *J. Phys. Chem.* **1975**, 79, 2525.
- (38) Egolf, D. S.; Waterland, M. R.; Kelley, A. M. *J. Phys. Chem. B* **2000**, 104, 10727.
- (39) Kelley, A. M.; Shoute, L. C. T.; Blanchard-Desce, M.; Bartholomew, G. P.; Bazan, G. C. *Mol. Phys.* **2005**, in press.
- (40) Frisch, M. J.; Trucks, G. W.; Schlegel, H. B.; Scuseria, G. E.; Robb, M. A.; Cheeseman, J. R.; Zakrzewski, V. G.; Montgomery, J. A., Jr.; Stratmann, R. E.; Burant, J. C.; Dapprich, S.; Millam, J. M.; Daniels, A. D.; Kudin, K. N.; Strain, M. C.; Farkas, O.; Tomasi, J.; Barone, V.; Cossi, M.; Cammi, R.; Mennucci, B.; Pomelli, C.; Adamo, C.; Clifford, S.; Ochterski, J.; Petersson, G. A.; Ayala, P. Y.; Cui, Q.; Morokuma, K.; Malick, D. K.; Rabuck, A. D.; Raghavachari, K.; Foresman, J. B.; Cioslowski, J.; Ortiz, J. V.; Baboul, A. G.; Stefanov, B. B.; Liu, G.; Liashenko, A.; Piskorz, P.; Komaromi, I.; Gomperts, R.; Martin, R. L.; Fox, D. J.; Keith, T.; Al-Laham, M. A.; Peng, C. Y.; Nanayakkara, A.; Gonzalez, C.; Challacombe, M.; Gill, P. M. W.; Johnson, B.; Chen, W.; Wong, M. W.; Andres, J. L.; Gonzalez, C.; Head-Gordon, M.; Replogle, E. S.; Pople, J. A. *Gaussian 98*; Revision A.7; Gaussian, Inc.: Pittsburgh, PA, 1998.
- (41) Myers, A. B.; Mathies, R. A. In *Biological Applications of Raman Spectroscopy*; Spiro, T. G., Ed.; Wiley: New York, 1987; Vol. 2, p 1.
- (42) Chung, Y. C.; Ziegler, L. D. *J. Chem. Phys.* **1988**, 88, 7287.
- (43) Mizuno, M.; Hamaguchi, H.; Tahara, T. *J. Phys. Chem. A* **2002**, 106, 3599.
- (44) Cho, M. *J. Phys. Chem. A* **1999**, 103, 4712.
- (45) Del Zoppo, M.; Bianco, A.; Zerbi, G. *Synth. Met.* **2001**, 124, 183.
- (46) Kirtman, B.; Champagne, B.; Bishop, D. M. *J. Am. Chem. Soc.* **2000**, 122, 8007.
- (47) Chernyak, V.; Tretiak, S.; Mukamel, S. *Chem. Phys. Lett.* **2000**, 319, 261.
- (48) Tripathy, K.; Moreno, J. P.; Kuzyk, M. G.; Coe, B. J.; Clays, K.; Kelley, A. M. *J. Chem. Phys.* **2004**, 121, 7932.
- (49) Bishop, D. M.; Luis, J. M.; Kirtman, B. *J. Chem. Phys.* **2002**, 116, 9729.
- (50) Kelley, A. M. *J. Chem. Phys.* **2003**, 119, 3320.
- (51) Kaatz, P.; Donley, E. A.; Shelton, D. P. *J. Chem. Phys.* **1998**, 108, 849.
- (52) Kato, Y.; Takuma, H. *J. Opt. Soc. Am.* **1971**, 61, 347.
- (53) Bischof, W. K.; Black, G. In *Excimer Lasers-1983*; Rhodes, C. K., Egger, H., Pummer, H., Eds.; American Institute of Physics: New York, 1983; p 181.
- (54) Dudik, J. M.; Johnson, C. R.; Asher, S. A. *J. Chem. Phys.* **1985**, 82, 1732.
- (55) Schomacker, K. T.; Delaney, J. K.; Champion, P. M. *J. Chem. Phys.* **1986**, 85, 4240.
- (56) Trulson, M. O.; Mathies, R. A. *J. Chem. Phys.* **1986**, 84, 2068.
- (57) Li, B.; Myers, A. B. *J. Phys. Chem.* **1990**, 94, 4051.
- (58) Leng, W.; Woo, H. Y.; Vak, D.; Bazan, G. C.; Kelley, A. M. *J. Raman Spectrosc.* **2005**, in press.
- (59) Myers, A. B. *Chem. Rev.* **1996**, 96, 911.